Proc. of the 32nd International Symposium on Shock Waves (ISSW32)
doi:10.3850/978-981-11-2730-4_0473-cd

Proper Orthogonal Decomposition of Streamwise-Velocity Fluctuations in a Compression-Corner Shock-Wave/Turbulent Boundary-Layer Interaction

M. A. Mustafa, N. J. Parziale
Department of Mechanical Engineering, Stevens Institute of Technology, Hoboken, NJ 07030, USA

Nick Parziale: nick.parziale@gmail.com

Abstract In this work, we use snapshot proper orthogonal decomposition (POD) to analyze shock-wave/turbulent boundary-layer interactions (SWBLI) in the compression-corner configuration. Using Krypton Tagging Velocimetry (KTV), we study the flow of a 99% N_2/1% Kr gas mixture over 8°, 16°, 24° and 32° compression corners at $M = 2.8$ and $Re_\Theta = 1750$. The experiments were performed in the AEDC Mach 3 Calibration Tunnel (M3CT) and the resulting KTV derived velocity fields are decomposed using POD to investigate the turbulent structure of the flows. From the POD results, we extract the dominant flow structures and compare each case by presenting mean-velocity maps that correspond to the largest positive and negative POD mode coefficients. This analysis allows us to relate POD modes with flow features such as separation, and also asses the effect of the wedge angle on the structure of the modes. Finally, the POD spectrum reveals an inertial range common to the incoming boundary-layer and each compression-corner flow that is present after the first ≈ 10 dominant POD modes.

1 Introduction

The interaction of shock waves and boundary layers is a fundamental problem in high-speed flow physics motivated by practical applications. Dolling [1] states "[shock-wave boundary-layer interactions] are ubiquitous in high-speed flight, occurring in an almost limitless number of external and internal flow problems relevant to aircraft, missiles, rockets, and projectiles. Maximum mean and fluctuating pressure levels and thermal loads that a structure is exposed to are generally found in regions of shock/boundary-layer and shock/shear-layer interaction and can [affect] vehicle and component geometry, structural integrity, material selection, fatigue life, the design of thermal protection systems, weight, and cost." Consequently, to better design high-speed vehicles it is necessary to understand the fundamentals of this complex interaction. This ubiquity has led to a plethora of computational [2, 3, 4, 5, 6] and experimental [7, 8, 9, 10, 11, 12] investigations into this interaction. Reviews [13, 14, 15] highlight the current state of the research.

The breadth of interactions is vast, as discussed in the introductory chapters of Babinsky and Harvey [16]. Furthermore, the presence of turbulence increases the complexity of SWBLI, by way of introducing additional time and length scales [17]. The interaction of this wide range of turbulent scales with a shock wave yields a rich, fundamental fluid-mechanics problem. Being able to quantify these scales and deepening our understanding of the physical properties and relative importance of these structures will further improve our ability to model turbulent flows. One analytical tool that accomplishes this is proper orthogonal decomposition (POD). It was first introduced to the fluid dynamics community by Lumley [18, 19] as a means to extract coherent structures from flow fields. A

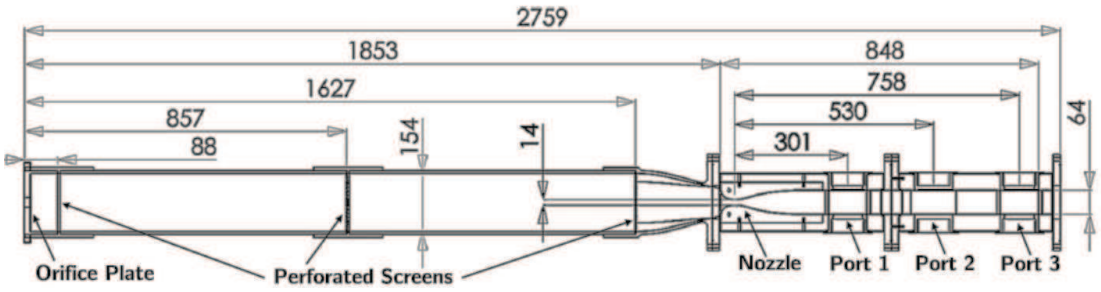

Fig. 1 Sketch of AEDC Mach 3 Calibration Tunnel (M3CT). Dimensions in millimeters. The measurements are made at "Port 2"

review of POD analysis in the broader context of modal analysis can be found in Taira et al. [20]. The fundamental idea of POD is to decompose the velocity field into a series of modes weighted based on the amount of kinetic energy they contain, each of which can be interpreted as a coherent structure. This technique has been used to study combustion engines [21, 22, 23], turbulent flow over a fence [24], open cavity flow [25], axisymmetric jet flow and mixing layers [26] and the turbulent flow over a cylinder [27], to name a few. There are not many applications of POD to SWBLIs in the literature. One example is that of Piponniau et al. [28] where a POD analysis was performed on PIV results from an induced-shock-wave/turbulent boundary-layer interaction. The authors aimed to investigate "the unsteady breathing of the recirculating bubble at low frequency and the Kelvin-Helmholtz instabilities developing at moderate frequency."

In this work, we focus our study on the effect of compression-corner angle on turbulent structure in Mach 2.8 flow. This canonical flow, for example, may be observed in practice as the deflection of a control surface on a vehicle in high-speed flight or in the flow path of a high-speed, air-breathing engine. We begin this paper by describing the experimental facility, the Mach 3 Calibration Tunnel (the M3CT), and the measurement technique, Krypton Tagging Velocimetry (KTV). Then, we report results in the form of fluorescence exposures, mean- and fluctuating-velocity profiles, and turbulent kinetic energy contours of flows over 8°, 16°, 24° and 32° compression corners. Finally, we apply POD to the KTV results and discuss the eigen-spectra and make case-wise comparisons of the most energetic POD modes.

2 Facility and Experimental Setup

The experiments were performed in the Arnold Engineering Development Complex (AEDC) Mach 3 Calibration Tunnel (M3CT) in Silver Spring, MD (Fig. 1). The tunnel is comprised of a large vacuum tank attached to a converging diverging nozzle. An orifice plate was added upstream of the nozzle as in Zahradka et al. [29] and Mustafa et al. [30] to control the freestream pressure. A flexible isolation bag was added upstream of the orifice to contain the 99% N_2/1% Kr gas mixture. The flexibility ensured that the bag stayed at the constant ambient pressure of the laboratory. A valve is cycled downstream of the nozzle to run the tunnel. The run condition calculations can be found in Zahradka et al. [29] and Mustafa et al. [30] (table 1).

To ensure that the M3CT started properly and to visualize the shock-wave/turbulent boundary-layer interaction structures, a Z-type schlieren setup [31] was used to visualize the flow field over the compression corners. The schlieren setup consisted of a sparklamp

Table 1 M_∞, P_∞, T_∞, ρ_∞, Re_∞^{unit}, Re_Θ, U_∞ and δ are the Mach number, pressure, temperature, density, unit Reynolds number, momentum-thickness Reynolds number, velocity and boundary-layer thickness for the AEDC M3CT tunnel with the 19.1 mm orifice plate. Additionally, u_τ, ν_w and η are the friction velocity, kinematic viscosity at the wall, and the viscous length, respectively. Values reported here are for "Port 2" in Fig. 1

M_∞ (-)	P_∞ (Pa)	T_∞ (K)	ρ_∞ (kg/m^3)	Re_∞^{unit} (1/m)	Re_Θ (-)	U_∞ (m/s)	δ (mm)	u_τ (m/s)	ν_w (m^2/s)	$\eta = \nu_w/u_\tau$ (µm)
2.77	1010	118	0.030	2.30e6	1750	612	10.25	34	0.0014	40

light source and an Integrated Design Tools N3 camera recording at 100 frames-per-second with a 50 ns exposure time. The knife-edge was set as a horizontal cutoff. Fig. 2 shows the mean of 100 exposures of the schlieren visualization for each wedge with the mean shock position marked, as determined by local curve fitting to the image intensity. Approximately 900 snapshots of data were collected for each geometry, which corresponds to a physical time of 90 s.

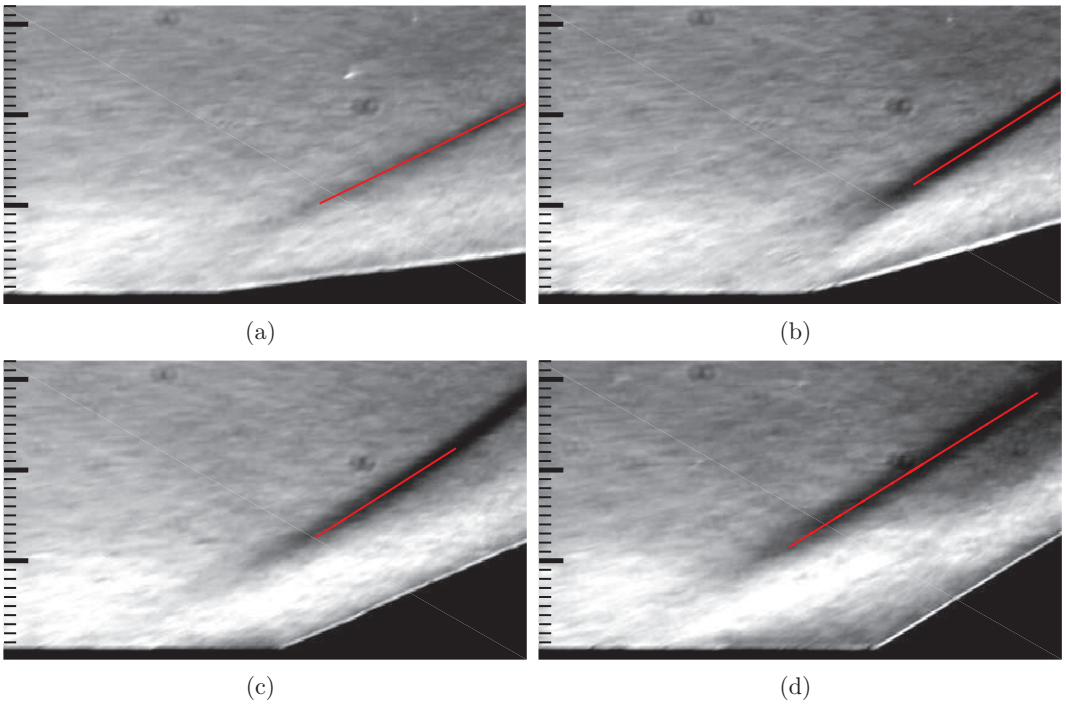

Fig. 2 Mean schlieren images for the (a) 8°, (b) 16°, (c) 24° and (d) 32° corners, respectively. Flow is left to right. Major tick marks are at 10 mm. Incoming boundary-layer thickness is $\delta = 10.25$ mm. Mean shock position shown in red

To compare the flow field investigated in the present work with that in the literature, the mean initial shock angles (β) are plotted in Fig. 3 against the wedge angle θ. The graph shows that for the 8° wedge, β is equal to the calculated value from inviscid theory. Beginning with the 16° wedge, β approaches a constant value of $\approx 32°$. This trend of β approaching a constant value is is in agreement with the work by Spaid and Frishett [32], which was experimental work performed at Mach 2.9. The value of β for the 8° and 16°

wedge is in agreement with previous work by Smits and Muck [10]. The initial shock angle for the 24° wedge is in agreement with DNS work by Wu and Martin [5] and experimental work by Settles et al. [8] and Mustafa et al. [30]. From the comparison of the initial shock angle with those in the literature, we conclude that the flow has started and these geometries can be studied in the M3CT.

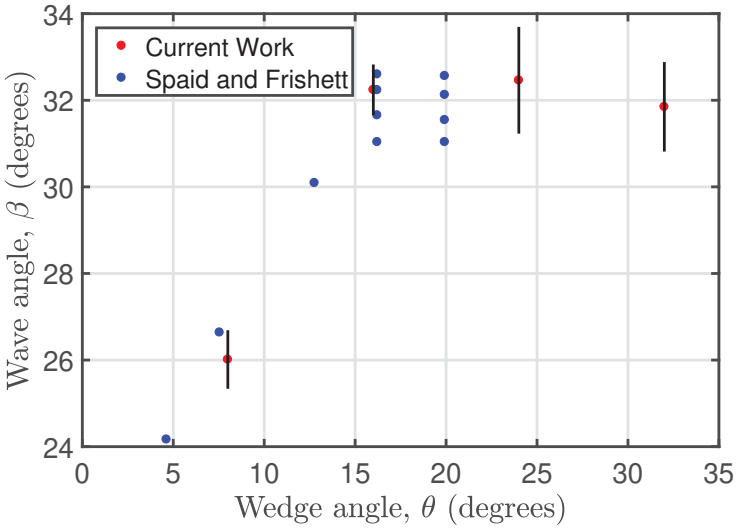

Fig. 3 Initial (β) shock angles from schlieren images shown in red. Results from Spaid and Frishett [32] shown in blue. Vertical black bars denote uncertainty

3 Diagnostic Approach: Tagging Velocimetry

Tagging velocimetry is a laser velocimetry technique which is typically performed in gases by tracking the fluorescence of a native, seeded, or synthesized gas. Its advantage over particle-based techniques in high-speed facilities is that it is not limited by timing issues associated with tracer injection [33] or reduced particle response at Knudsen and Reynolds numbers [34] characteristic of high-speed wind tunnels. Methods of tagging velocimetry include the VENOM [35, 36, 37, 38, 39], APART [40, 41, 42], RELIEF [43, 44, 45, 46, 47], FLEET [48, 49], STARFLEET [50], PLEET [51], argon [52], iodine [53, 54], sodium [55], acetone [56, 57, 58], NH [59] and the hydroxyl group techniques, [60, 61, 62, 63] among others [64, 65, 66, 67, 68, 69].

For this work, Krypton Tagging Velocimetry (KTV) was used as the velocimetry technique. The use of a metastable noble gas as a tagging velocimetry tracer was first suggested by Mills et al. [70] and Balla and Everhart [71]. KTV was first demonstrated by Parziale et al. [72, 73] to measure the velocity along the center-line of an underexpanded jet of N_2/Kr mixtures. Following that work, Zahradka et al [74, 29] used KTV to make measurements of the mean and fluctuating turbulent boundary-layer profiles in a Mach 2.8 flow. Mustafa et al. [75] used KTV to measure ≈ 20 simultaneous profiles of streamwise velocity and fluctuations in the incoming boundary layer and flow over 8°, 16°, 24° and 32° compression corners in $M_\infty = 2.8$, $Re_\Theta = 1750$, 99% N_2/1% Kr shock-wave/turbulent boundary-layer interactions. Recently, KTV was implemented in the Stevens Institute of Technology Shock Tube by Mustafa et al. [76] to measure the freestream velocity behind a Mach 4.5 shock in 99% N_2/1% Kr and 75% N_2/20% O_2/5% Kr gas mixtures. In

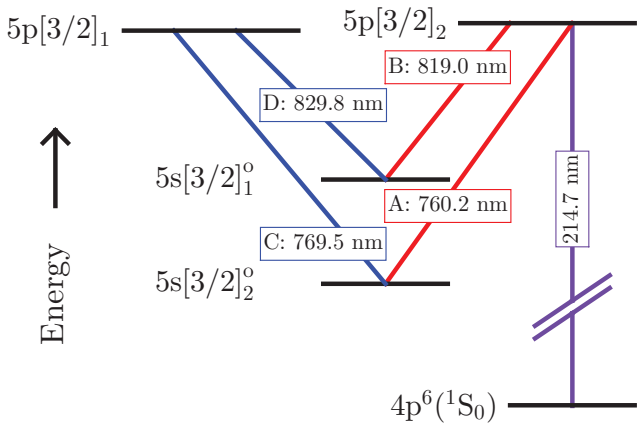

Fig. 4 Energy diagram for excitation scheme. Racah nl[K]$_J$ notation, A, B, C and D represent the transitions between the states

addition, KTV has been demonstrated to work in the freestream of the large-scale AEDC Hypervelocity Tunnel 9 at Mach 10 and Mach 14 [77].

Following the excitation scheme used by Mustafa et al. [30], KTV is performed in the following steps according to the energy level diagram shown in Fig. 4.

(i) Seed a base flow with krypton globally, in this case 1% Kr in 99% N_2.

(ii) Photosynthesize metastable krypton atoms with a pulsed tunable laser to form the tagged tracer: two-photon excitation of $4p^6(^1S_0) \rightarrow 5p[3/2]_2$ (214.7 nm) and rapid decay to resonance state $5p[3/2]_2 \rightarrow 5s[3/2]^o_1$ (819.0 nm, transition B) and metastable state $5p[3/2]_2 \rightarrow 5s[3/2]^o_2$ (760.2 nm, transition A). We estimate that the creation of the metastable atoms which comprise the "write line" takes approximately 50 ns [78]. The position of the write line is marked by the fluorescence from the $5p[3/2]_2 \rightarrow 5s[3/2]^o_1$ transitions (819.0 nm, transition B), and is recorded with a camera positioned normal to the flow.

(iii) Record the displacement of the tagged metastable krypton by imaging the laser induced fluorescence (LIF) that is produced with an additional pulsed tunable laser: excite $5p[3/2]_1$ level by $5s[3/2]^o_2 \rightarrow 5p[3/2]_1$ transition with laser sheet (769.5 nm, transition C) and read spontaneous emission of $5p[3/2]_1 \rightarrow 5s[3/2]^o_1$ (829.8 nm, transition D) transitions with a camera positioned normal to the flow.

The experiments were run using two tunable lasers to provide the 214.7 nm (write) and 769.5 nm (read) laser beams required for KTV. The write laser consisted of a frequency doubled Quanta Ray Pro-350 Nd:YAG laser and a frequency tripled Sirah PrecisionScan Dye Laser. The Nd:YAG laser pumped the dye laser with 1000 mJ/pulse at a wavelength of 532 nm. The dye in the laser was DCM with a dimethyl sulfoxide (DMSO) solvent, and the laser was tuned to output a 644.1 nm beam. Frequency tripling of the dye-laser output was performed using Sirah tripling optics (THU 205).

The write-laser beam setup can result in approximately 10-13 mJ/pulse; however, approximately 7 mJ was used for this experiment by reducing the Nd:YAG pump-laser power. The wavelength was 214.7 nm, with a linewidth of approximately 0.045 cm^{-1}, a pulsewidth of approximately 7 ns, and a repetition rate of 10 Hz. The write beam was focused into several narrow waists in the test section with a $f = 100$ mm fused-silica

microlens array (SUSS MicroOptics Nr. 18-00127) to form the lines in the streamwise direction and a $f = 100$ mm fused-silica cylindrical lens to focus the lines in the spanwise direction. We estimate that the energy per write line was approximately 350 µJ/pulse.

The read laser consisted of a frequency doubled Quanta Ray Pro-350 Nd:YAG laser and a Sirah PrecisionScan Dye Laser. The Nd:YAG laser pumped the dye laser with 200 mJ/pulse at a wavelength of 532 nm. The dye in the laser was Styryl 8 with a DMSO solvent, and the laser was tuned to output a 769.5 nm beam.

The read-laser beam setup resulted in approximately 5 mJ/pulse, with a wavelength of 769.5 nm, a linewidth of approximately 0.025 cm^{-1}, a pulsewidth of approximately 7 ns, and a repetition rate of 10 Hz. The read-laser beam was directed into the test section using 2 inch broadband dielectric mirrors (Thorlabs BB2-E02), and expanded to a beam of ≈ 40 mm diameter with a $f = -400$ mm BK7 lens. This "read beam" re-excited the metastable Kr tracer atoms so that their displacement could be measured.

The laser and camera timing were controlled by a pulse-delay generator (SRS DG645). The intensified camera used for all experiments was a 16-bit Princeton Instruments PIMAX-4 1024x1024 with an 18-mm grade 1, Gen III extended red filmless intensifier w/ P46 phosphor (PM4-1024i-HR-FG-18-P46-CM). The lens used is a Nikon NIKKOR 24-85mm f/2.8-4D in "macro" mode and positioned approximately 200 mm from the write/read location which was at the center of the test section at Port 2 in Fig. 1. Two high-precision 800 nm longpass filters (Thorlabs FELH0800, transmission of 3.5e-4% at the read-laser wavelength of 769.5 nm) were placed in series between the lens and the intensifier to minimize the noise resulting from the read-laser pulse reflection and scatter from solid surfaces. The gain was set to 100% with 1x6 (streamwise x wall-normal) pixel binning and only recording the read images to ensure a 10 Hz frame rate. A set of write images were recorded with the tunnel on prior to each set of experiments. The camera gate was opened for 20 ns immediately following the read-laser pulse to capture the spontaneous emission of $5p[3/2]_1 \rightarrow 5s[3/2]_1^o$ (829.8 nm) transitions.

4 Shock-Wave/Turbulent Boundary-Layer Interaction Results

In this section, we present the results from experiments designed to investigate turbulent, supersonic corner flows at four different angles: 8°, 16°, 24°, and 32°. This is done by fixing a wedge of the appropriate geometry in Port 2 of the M3CT (see Fig. 1).

Fig. 5 shows sample KTV read exposures for each case. This is the visualization of the $5p[3/2]_1 \rightarrow 5s[3/2]_1^o$ (829.8 nm) transitions. Mach 2.8 flow is left to right and the walls in each corner flow are marked in black. To process the KTV exposures, the line centers were found in the following way:

1) Crop the image to an appropriate field of view.

2) Apply a two-dimensional Wiener adaptive-noise removal filter.

3) Convert the images to double precision numbers and normalize the intensity to fall in the range of 0-1.

4) Apply the Gaussian peak finding algorithm from [79] to find the line centers for the top row using the read lines in the top row of each image as a first guess.

5) Proceeding from the top-down, apply the Gaussian peak finding algorithm from O'Haver [79] to find the line centers for each row using the line center location immediately above as the guess.

Examples of non-dimensional instantaneous velocity profiles ($u/(12U_\infty)$) are presented in Fig. 6. For each corner angle, we show the write location marked as a thin, vertical

black line and two randomly selected, example instantaneous velocity profiles in blue and red. This is intended to visualize relative unsteadiness of each corner flow. Results are not presented within $y/\delta < 0.1$ because the signal to noise ratio was too low to provide data with high confidence. In addition, there is a missing velocity profile every 10 mm

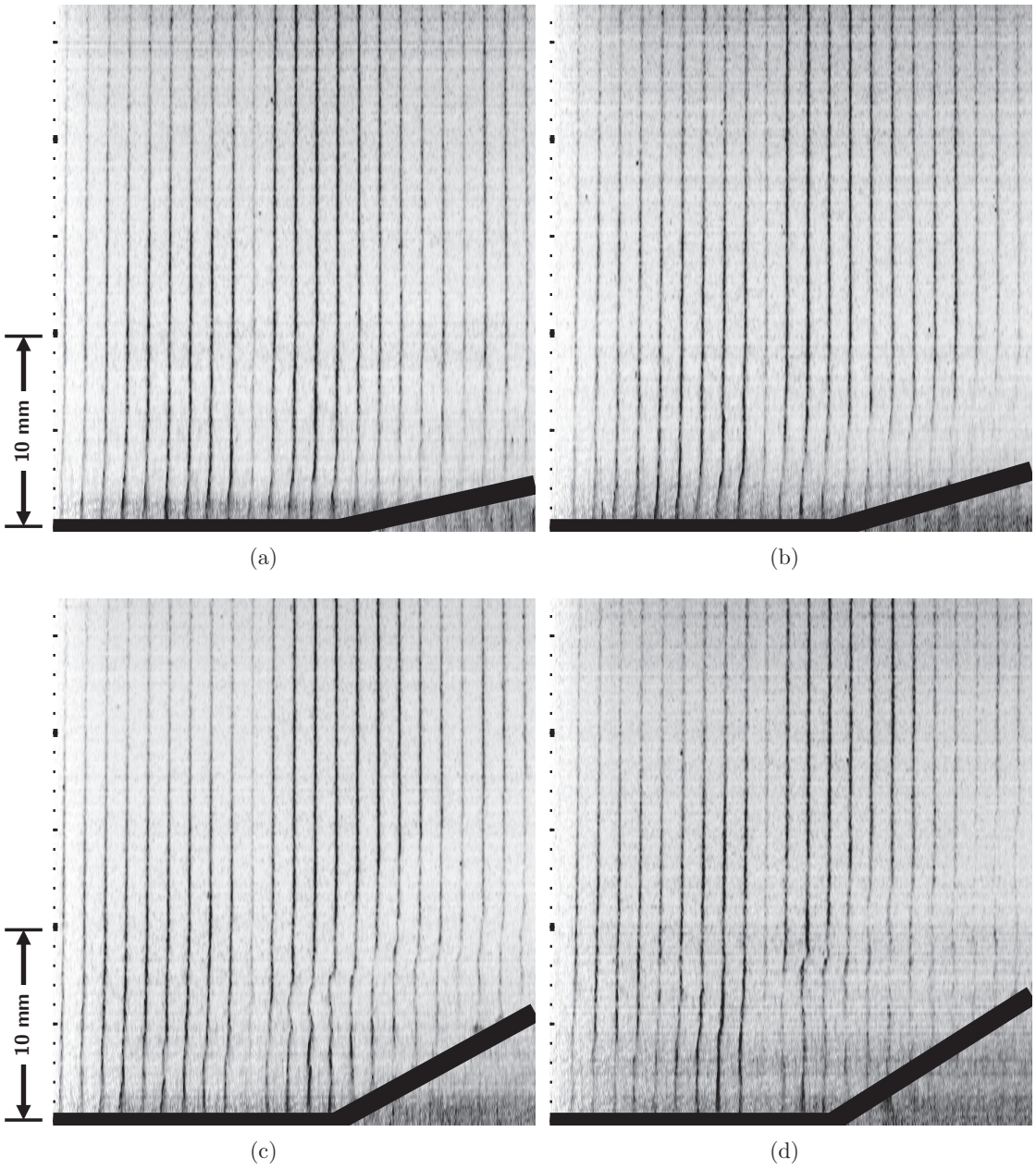

Fig. 5 Sample instantaneous shock-wave/turbulent boundary-layer interaction fluorescence exposures for the (a) 8°, (b) 16°, (c) 24° and (d) 32° corners, respectively. These are ostensibly boundary-layer profiles traces with a 500 ns prescribed delay between the write and read step. Major tick marks are 10 mm. Flow is left to right. Inverted intensity scale. Wall marked as black

because there is a gap between the microlens arrays that yields insufficient focusing and thus low SNR.

In Fig. 7, we present non-dimensional mean velocity profiles ($u/(12U_\infty)$). For each corner angle, we show the write location marked as a thin, vertical black line and the mean velocity profile as a thicker blue line. In the 8° and 16° cases, there are no clearly apparent points of inflection in mean profiles. In the 24° case, near to the root ($-0.5 \lesssim x/\delta \lesssim 0.5$), and to a much greater extent in the 32° case (the field of view), there appear to be clear points of inflection in the mean boundary-layer profiles.

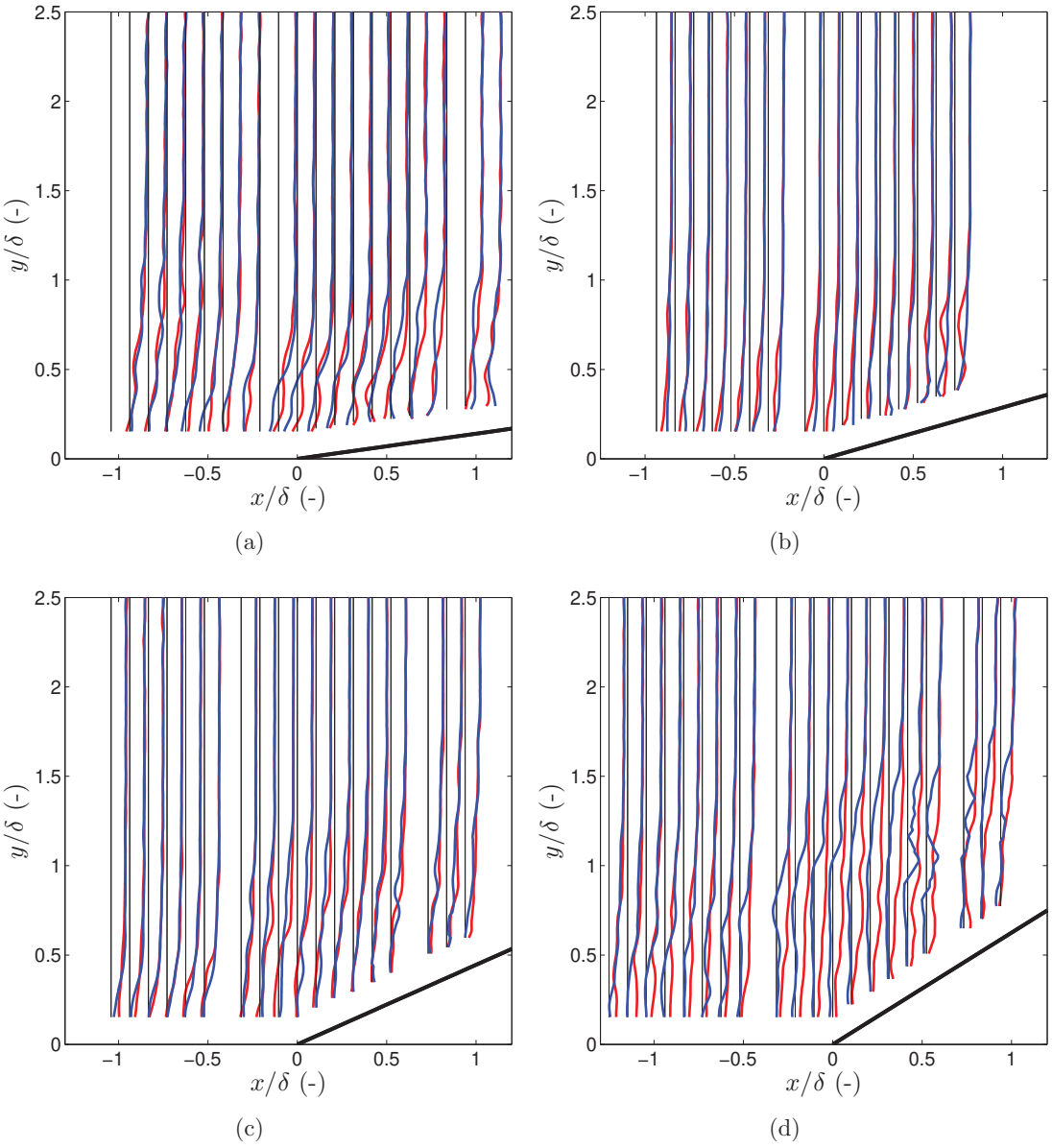

Fig. 6 Sample non-dimensional ($u/(12U_\infty)$), instantaneous shock-wave/turbulent boundary-layer interaction velocity profiles represented in blue and red for the (a) 8°, (b) 16°, (c) 24° and (d) 32° corners, respectively. Thin vertical black line represents the write location. Flow is left to right

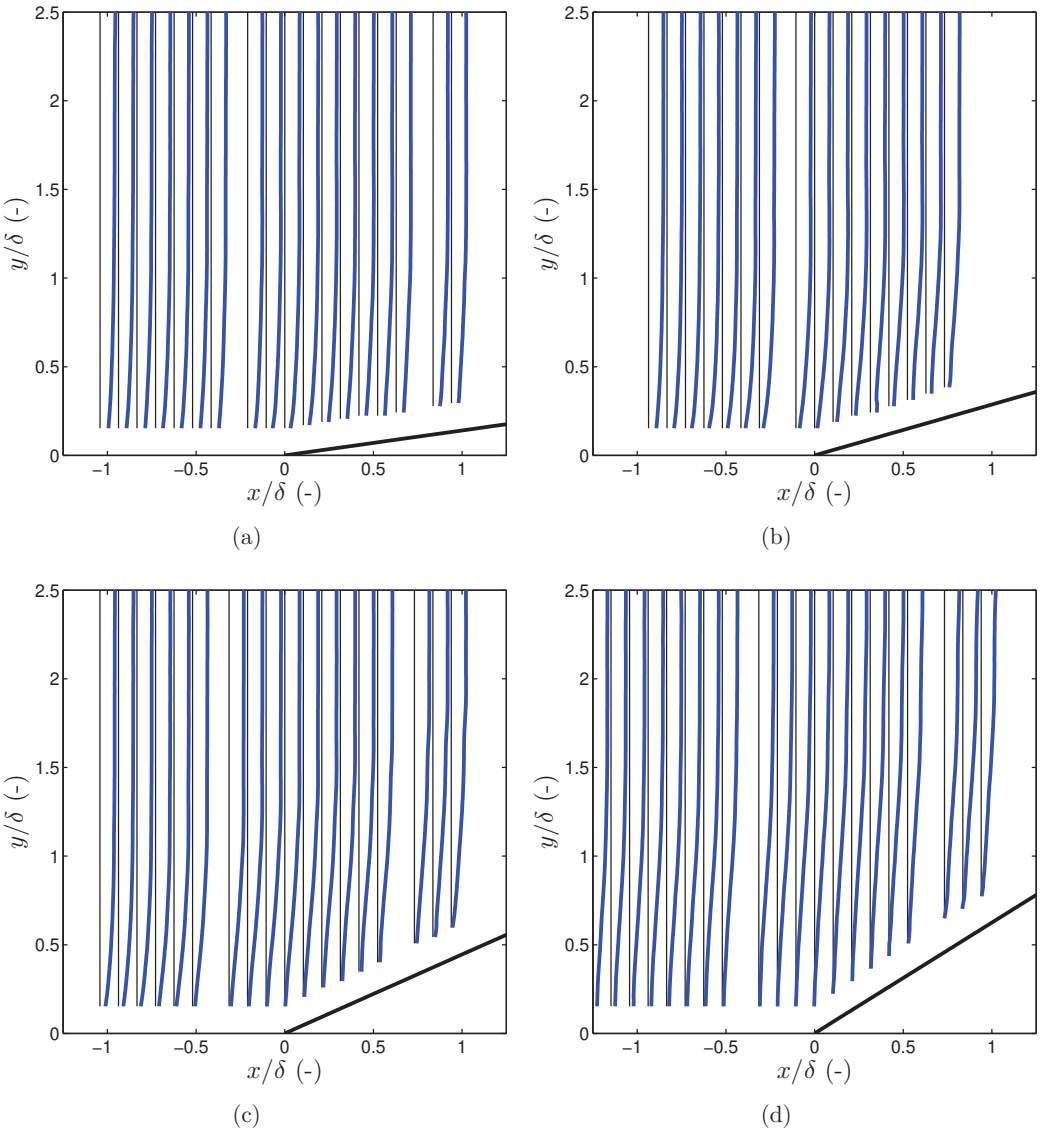

Fig. 7 Non-dimensional ($u/(12U_\infty)$), mean shock-wave/turbulent boundary-layer interaction velocity profiles for the (a) 8°, (b) 16°, (c) 24° and (d) 32° corners, respectively. Thin vertical black line represents the write location. Flow is left to right. Error bars are not plotted because they are not visible at the present scale. We estimate the uncertainty as 5% in the freestream and 15% near the wall

Contours of the streamwise component of turbulent kinetic energy (sTKE), $(u'_{RMS})^2/(2U_\infty^2)$, are presented in Fig. 8. For each case, very close to the wall on the ramp, there is a notable increase in fluctuations. This is most likely an artifact of the residual noise from the KTV read step. Despite this, in the 16°, 24° and 32° cases, a shear layer can clearly be identified as a maximum in fluctuations along a ray inclined at an angle similar to that of the corner angle. No such shear layer was observed in the 8° case.

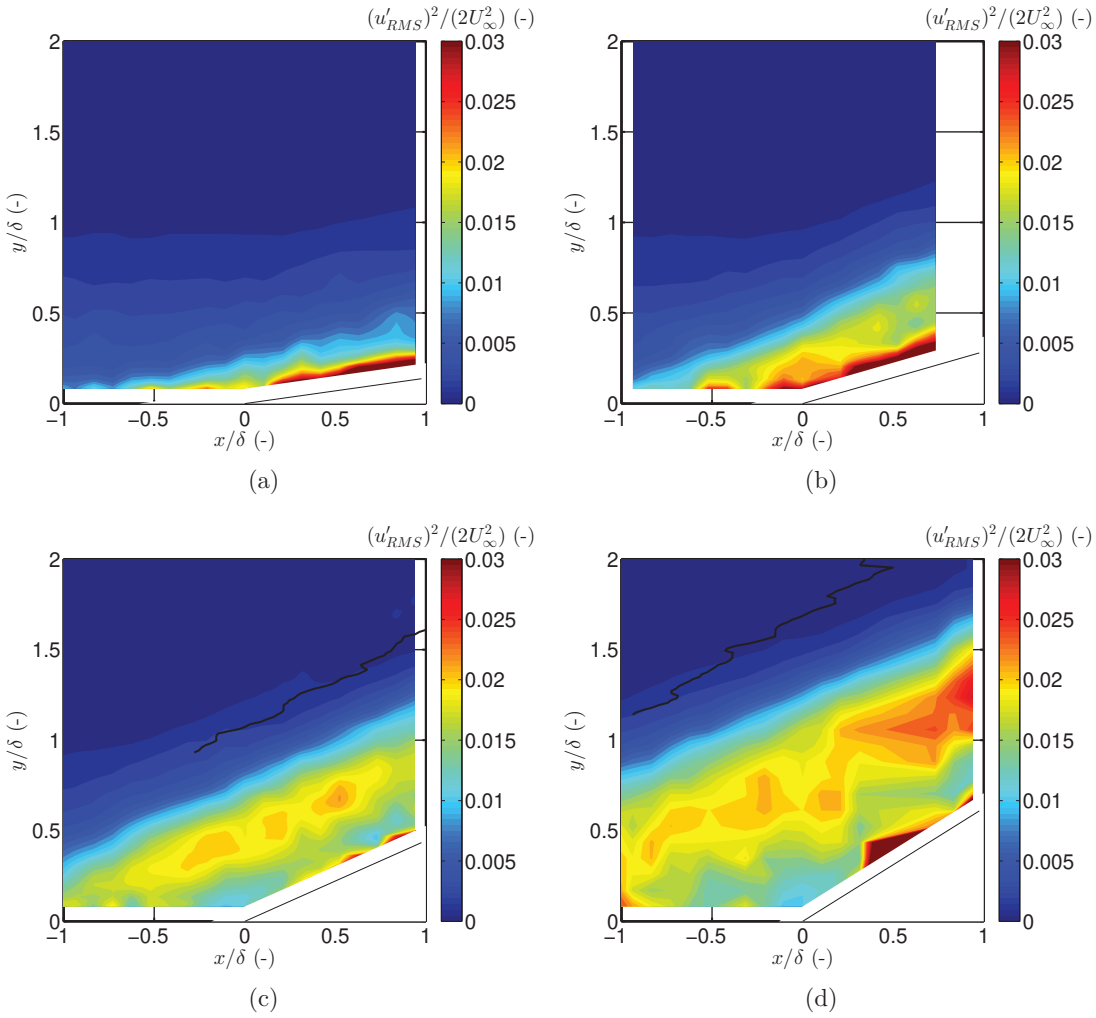

Fig. 8 Countours of the non-dimensional streamwise turbulent kinetic energy (sTKE) $(u'_{RMS})^2/(2U_\infty^2)$) for the (a) 8°, (b) 16°, (c) 24° and (d) 32° corners, respectively. Flow is left to right. Mean shock position shown in black

5 Proper Orthogonal Decomposition

The proper orthogonal decomposition (POD) technique can be used to extract spatial and temporal structures from a turbulent flow field [18, 19, 20]. This approach decomposes the original vector or scalar field into a weighted, linear sum of basis functions, or modes. In the present work, the instantaneous streamwise velocity fields are recorded at 10 Hz so they are nominally uncorrelated in time; thus, the snapshot method of Sirovich [80] was chosen to analyze the data.

Following the terminology in Sirovich [80] and Stöhr [81], the streamwise velocity fields are decomposed into a mean and fluctuating component as

$$u_i(x,y) = \overline{u}(x,y) + u'_i(x,y). \tag{1}$$

In the datasets presented here, there are p points in the streamwise direction and q points in the wall-normal direction ($M = p \times q$ total grid points) with N number of snapshots ($i = 1....N$). The fluctuating streamwise velocity field, $u'_i(x,y)$, is reshaped into a matrix,

$\mathbf{U}'$, with elements $U_i'(X_n)$ where the $n = 1....M$ points for each snapshot form a row for $i = 1....N$ rows, so $\mathbf{U}'$ is of dimensions $N \times M$ and can be written as

$$\mathbf{U}' = \begin{bmatrix} u_1'(x_1,y_1) & u_1'(x_2,y_1) & .. & u_1'(x_p,y_q) \\ u_2'(x_1,y_1) & u_2'(x_2,y_1) & .. & u_2'(x_p,y_q) \\ : & : & .. & : \\ : & : & .. & : \\ u_N'(x_1,y_1) & u_N'(x_2,y_1) & .. & u_N'(x_p,y_q) \end{bmatrix} = \begin{bmatrix} U_1'(X_1) & U_1'(X_2) & ... & U_1'(X_M) \\ U_2'(X_1) & U_2'(X_2) & ... & U_2'(X_M) \\ : & : & ... & : \\ : & : & ... & : \\ U_N'(X_1) & U_N'(X_2) & ... & U_N'(X_M) \end{bmatrix}. \quad (2)$$

Where $U_1'(X_2)$ is the value of u' at the spatial location X_2 in the 1^{st} snapshot and so on, We assume that velocity may be written as

$$U_i'(X_n) = \sum_{j=1}^{N} a_{ij}\phi_j(X_n). \quad (3)$$

Here, $\phi_j(X_n)$ is the j^{th} eigenfunction (or mode) and a_{ij} is the coefficient of the of the j^{th} mode that corresponds to the i^{th} snapshot of the velocity field. The goal is to prescribe a condition that would allow us to identify flow structures within a mode ϕ_j. The condition that achieves this, following Berkooz et al. [19], is that the decomposition be optimal. Optimal here means that for a given number of modes, the decomposition will contain the most kinetic energy possible out of all possible decompositions. When this condition is met, the decomposition in Eq. (3) will represent the proper orthogonal decomposition. To impose the optimality condition, the Fredholm integral eigenvalue problem must be solved,

$$\int_{\Omega} R(X_m, X_n)\phi_j(X_n)d\Omega = \overline{\lambda}\phi_j(X_m). \quad (4)$$

Here, m is a free index ($m = 1....M$), $\overline{\lambda}$ is the eigenvalue of mode j and Ω is the region of integration, which is the flow field space. $R(X_m, X_n)$ is the two-point correlation defined as,

$$R(X_m, X_n) = \overline{U'(X_m)U'(X_n)} \quad (5)$$

To solve the eigenvalue problem, the integral in Eq. (4) must be approximated by a finite sum. This is accomplished by writing

$$\sum_{n=1}^{M} R(X_m, X_n)\phi_j(X_n)\Delta\Omega_n = \overline{\lambda}\phi_j(X_m). \quad (6)$$

Here, we have divided the domain into M subdivisions, each of size $\Delta\Omega_n$. Each subdivision encompasses a spatial (measurement) location X_n. To solve the eigenvalue problem in MATLAB, the matrix $\mathbf{R}$, whose elements are $R(X_m, X_n)$, can be constructed from $\mathbf{U}'$ as,

$$\mathbf{R} = \frac{1}{N}\mathbf{U}'^T\mathbf{U}' \quad (7)$$

and the superscript T denotes the matrix transpose. The dimensions of $\mathbf{R}$ are $M \times M$. Using this, the eigenvalue problem of Eq. (6) can be written as,

$$\mathbf{R}\overline{\mathbf{W}}\boldsymbol{\phi_j} = \overline{\lambda}\boldsymbol{\phi_j}. \quad (8)$$

Here $\overline{\mathbf{W}}$ is a diagonal matrix of dimensions $M \times M$ which contains the $\Delta\Omega_n$ values for all the spatial locations and $\boldsymbol{\phi_j}$ is a $M \times 1$ column vector whose elements are $\phi_j(X_n)$

$(n = 1....M)$. From $\overline{\mathbf{W}}$ can can extract a constant $\Delta\Omega$ and can write the eigenvalue problem as,

$$\Delta\Omega\mathbf{R}\mathbf{W}\boldsymbol{\phi_j} = \overline{\lambda}\boldsymbol{\phi_j}. \tag{9}$$

Now $\mathbf{W}$ contains the spatial weights of each location relative to the constant $\Delta\Omega$ and has no units. Furthermore, we can combine $\Delta\Omega$ with the eigenvalue ($\lambda = \overline{\lambda}/\Delta\Omega$) to write,

$$\mathbf{R}\mathbf{W}\boldsymbol{\phi_j} = \lambda\boldsymbol{\phi_j}. \tag{10}$$

Note that the eigenvalue λ has units of $\mathrm{m^2s^{-2}}$ in this work. Eq. (10) represents the general eigenvalue problem and can be solved once $\mathbf{W}$ is determined. In the case of this work, the laser lines are evenly spaced except at two locations in the flow field. These locations correspond to the missing velocity profiles because of the gap in the microlens array. Therefore the spatial points in the two laser lines adjacent to the missing line have to be weighted by a factor of 1.5 more than all the other points in order to integrate over the entire domain. However it was found that, by neglecting or adding the different spatial weights of the aforementioned points, the changes in the results were negligible, therefore in this work $\mathbf{W}$ was the identity matrix and the eigenvalue problem further simplifies to,

$$\mathbf{R}\boldsymbol{\phi_j} = \lambda\boldsymbol{\phi_j}. \tag{11}$$

The dimensions of $\mathbf{R}$ are $M \times M$, which in this work is $\approx 2500\times2500$. This a fairly large matrix whose eigenvalue computation is expensive. To address this computational cost, Sirovich [80] suggested solving the following nominally equivalent eigenvalue problem,

$$\mathbf{C}\boldsymbol{e_j} = \lambda\boldsymbol{e_j}. \tag{12}$$

Where $\mathbf{C} = (1/N)\mathbf{U}'\mathbf{U}'^T$, with dimensions of $N \times N$ and $\boldsymbol{e_j}$ is the eigenfunction (represented here as a column vector). In this work $N \approx 900$ and therefore Eq. (12) is less computationally expensive than Eq. (11). The POD modes can be derived from Eq. (12) as [81],

$$\phi_j(X_n) = \frac{1}{\lambda_j N}\sum_{i=1}^{N} a_{ij}U_i'(X_n). \tag{13}$$

The mode coefficients a_{ij} are,

$$a_{ij} = e_{ij}\sqrt{\lambda_j N}. \tag{14}$$

The POD modes form an orthonormal set and are normalized such that,

$$\boldsymbol{\phi_i}\cdot\boldsymbol{\phi_j} = \delta_{ij}, \tag{15}$$

where δ_{ij} is the Kronecker delta and "$\cdot$" denotes the vector dot product. The eigenvalues have special significance because,

$$E_{tot} = \sum_{n=1}^{M}\overline{R(X_n, X_n)} = \sum_{j=1}^{N}\lambda_j \tag{16}$$

Consequently, each eigenvalue represents the contribution of its corresponding mode to the total energy, and in the discussion of results, the energies (λ_j), will be normalized by this E_{tot}.

It should be noted that in the preceding formulation, thermodynamic variables are not considered because none were measured in these experiments. Sirovich [80] and Rowley [82] state that in a compressible flow, both the velocity and thermodynamic variables are dynamically important and should be included in the analysis. In this work, only the streamwise velocity fluctuations are measured and so the analysis is limited in this sense. However, researchers have used POD of single components of velocity to successfully examine the structure of compressible turbulent flows. For example, Murray et al. [25] used the vertical component of velocity to study the structure of subsonic open cavities. To estimate the effect of a compressible flow field to a first approximation, the density field is broken into pre- and post-shock values. The first value is the value in the freestream and the second is calculated from the oblique shock relations with the shock position serving as a demarcation line. Then, POD analysis is carried out for $\sqrt{\rho}u'$ (instead of u'), which results in eigenvalues that are representative of $\rho u'^2$, which is the turbulent kinetic energy. However, we observed that this correction did not significantly alter the structure and spectrum of the POD modes for these experiments; hence, the formulation without the density was used.

6 Eigenvalues of Snapshot POD Analysis

In this section, we present and discuss the eigenvalue results from applying the snapshot POD method to the KTV data reported in earlier sections. In Fig. 9(a), we present the cumulative fractional energy versus mode number. For each case, the first mode accounts for $\approx 20-30\%$ of the E_{tot} (Eq. (16)) and the first 6-10 modes capture approximately 60% of the E_{tot} in the flow. No clear trends as to the fraction of energy of the first mode or the cumulative fractional energy can be found between the different flow-fields investigated in this work.

The eigenvalue spectrum is plotted for each case in Fig. 9(b). Knight and Sirovich [83] and Moser [84] suggest that the POD eigenfunctions are a good set of basis functions with which to form an inertial-range spectrum for inhomogeneous, turbulent flows, as is the case here. The famous inertial-range scaling due to Kolmogorov [85] is

$$E \propto \epsilon^{2/3} k^{-5/3}, \tag{17}$$

where E is the energy per scalar wavenumber, ϵ is the dissipation rate, and k is the wavenumber. Stated equivalently

$$\mathscr{E} \propto \epsilon^{2/3} k^{-11/3}, \tag{18}$$

where $\mathscr{E}$ is the energy per vector wavenumber. Knight and Sirovich [83] argue that the wave number is proportional to the mode number as $k \propto j^{1/3}$, and so in the inertial range the eigenvalues scale as

$$\lambda_j \propto j^{-11/9}, \tag{19}$$

which is represented in Fig. 9(b) as a dashed line. Knight and Sirovich [83] also state that the inertial range will be shorter by a factor of three in equivalent wave number space (measured in decades). The differences between the different spectra presented here are modest for mode numbers $j < 100$, above which the noise from the measurement technique may play a role.

The authors initially expected an appreciably different eigenvalue spectrum when comparing each case because of how dissimilar and inhomogeneous the flow fields are. For

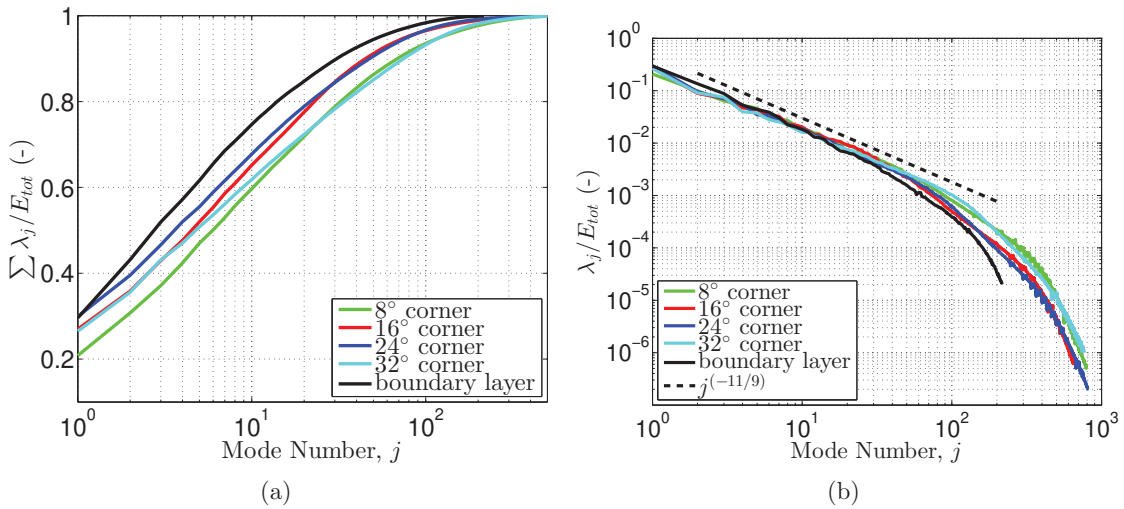

Fig. 9 (a) The cumulative fraction of energy, $\sum \lambda_j/E_{tot}$. (b) The fraction of energy of each mode, λ_j/E_{tot}. The black line is the mode number raised to the (-11/9) power as suggested in Knight and Sirovitch [83]

example, the 32° corner flow is inhomogeneous in the streamwise and wall-normal directions and has a relatively large separated region. This is in contrast to the boundary-layer flow, which is attached and inhomogeneous in only the wall-normal direction, yet the spectra are similar. However, upon close inspection, the first few POD modes do not clearly scale as $j^{-11/9}$, and these modes contain the structures (inhomogeneity and separation) which strongly modify the mean flow; this will be evident in the forthcoming presentation of the POD modes.

This scaling of the eigenvalues is similar to that found in Piponniau et al. [28] where a POD analysis was performed on PIV results from an induced-shock-wave/turbulent boundary-layer interaction. Piponniau et al. [28] report a smaller observed value of the roll off ($\lambda \propto j^{-0.9}$) which may be due to the fact that: 1) the flow field is not the same (impinged-shock/boundary-layer interaction vs. corner flow); 2) it is understood that the wall-normal component of fluctuating velocity tends to have a flatter spectrum in high-speed wall-bounded boundary layers than does the streamwise component Brooks et al. [86] and Piponniau et al. [28] utilized both streamwise and wall-normal velocities in their analysis vs. only streamwise in the present analyis; and 3) the measurement technique was PIV in Piponniau et al. [28] vs. KTV in the present work.

7 POD Coefficients and Modes of 24-degree Corner Flow

Here, we will discuss the 24° corner flow case in detail because it is often explored in other literature. In Fig. 10(a), we present the first POD mode coefficients ($a_{i1}/\sqrt{E_{tot}}$) for the 24° corner flow. We do not observe any clear trends in time for this or any POD mode. Additionally, we do not observe any clear phenomena when constructing phase portraits (two different POD mode coefficients plotted against one another), or transforming the POD mode coefficients into frequency space. One reason for not observing any interesting phenomena, such as the low-frequency dynamics discussed in Clemens and Narayanaswamy [87], is a lack of temporal resolution. The laser repetition rate for this experiment is fixed to 10 Hz dictating a Nyquist frequency of 5 Hz, which is far slower

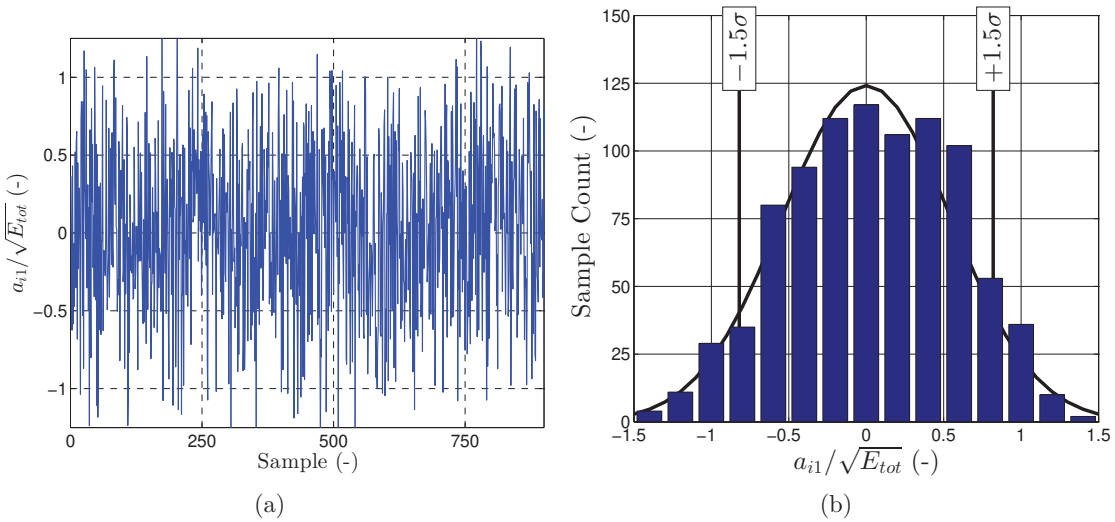

Fig. 10 First POD mode coefficients for 24° corner flow. (a) Coefficients for POD mode $j = 1$, a_{i1} vs. sample number. (b) Sample distribution of coefficients for mode $j = 1$. Vertical black bars mark 1.5 standard deviations (1.5σ) indicating large magnitude coefficients $|a_{i1}|$

than the characteristic time scales of this flow.

The sample distribution of energy for the first POD mode of the 24° corner flow is presented in Fig. 10(b). There are no observable biases about the mean to within experimental error. Also in Fig. 10(b), we mark the locations corresponding to 1.5 standard deviations (1.5σ) of the $|a_{i1}|$ samples which have the largest magnitude; we will use the samples that correspond to these large coefficient values (positive and negative) to gain insight into the mean-flow behavior exhibited by the POD modes.

The first six POD modes for the 24° corner flow are shown as contours of ϕ_j in the first row of Fig. 11. To illustrate the effect of the different POD modes on the mean-flow, the mean streamwise velocity of snapshots that correspond to the largest positive and negative mode coefficients is presented in the second and third rows of Fig. 11, respectively. That is, in the second row of Fig. 11, we present the mean of the streamwise velocity of the snapshots corresponding to samples falling above 1.5 standard deviations of the POD mode coefficient distribution ($+1.5\sigma$ of a_{i1}). And, in the third row of Fig. 11, we present the mean of the streamwise velocity of the snapshots corresponding to samples falling below 1.5 standard deviations of the POD mode coefficient distribution (-1.5σ of a_{i1}).

The first POD mode, ϕ_1, of the 24° corner flow case appears in the first row of the first column in Fig. 11. Inspecting the mean velocity field associated with large values of the mode coefficients, it appears that this POD mode is associated with large-scale filling ($+1.5\sigma$ of a_{i1}, second row, first column of Fig. 11) and complete collapse (-1.5σ of a_{i1}, third row, first column of Fig. 11) of the separation bubble at the root of the corner. The second POD mode, (ϕ_2, second column of first row) appears to be the separation bubble oscillating in the streamwise direction as evidenced by the POD mode and the associated mean velocity fields associated with the large mode coefficients ($\pm 1.5\sigma$ of a_{i2}). It appears that there is a sloshing, or shift in the streamwise direction of high and low momentum fluid. The third POD mode (ϕ_3, third column of first row) appears to be smaller-scale separation-bubble filling and collapse in comparison with ϕ_1. There is an

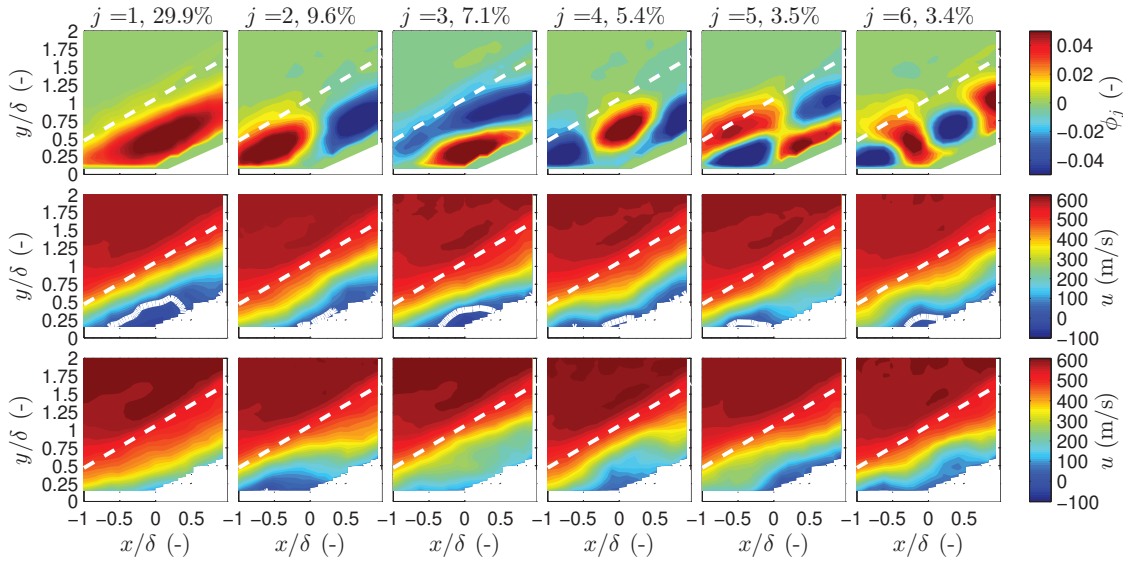

Fig. 11 Snapshot POD analysis for the 24° corner flow. Each column corresponds to one of the first six POD modes marked by the mode number j and the fraction of energy associated with each mode in %. Top row: POD modes for the 24° corner flow are shown as contours of ϕ_j. Middle row: the mean streamwise velocity of snapshots with the largest positive mode coefficients (samples falling to right of $+1.5\sigma$ in Fig. 10). Bottom row: the mean streamwise velocity of snapshots with the largest negative mode coefficients (samples falling to left of -1.5σ in Fig. 10). A solid white line denotes the boundary between positive and negative streamwise velocity. A dashed white line denotes the mean shock location

additional flow feature: when the flow is separated, there is a momentum surplus in the region immediately above the separation location and when the separation bubble is collapsed, there is a momentum deficit in the same region. This is potentially indicative of snapshots where the separation bubble is in the process of filling or collapsing. Modes ϕ_4 and ϕ_5 (fourth and fifth column of first row, respectively) appear to be harmonics of modes ϕ_2 and ϕ_3, respectively. Mode ϕ_6 (sixth column of first row, respectively) is difficult to interpret, but could be a harmonic of ϕ_4. Higher order modes, not pictured here, indicate increasingly smaller structures within the boundary layer and shock layer. In some of the higher modes, there are thin structures which appear close to the mean shock location, but these structures are associated with POD modes containing less than 1% of the TKE in the flow. That is, the energy associated with fluctuations from the mean-shock location are small relative to the fluctuations associated with the dynamics of the separation bubble.

8 Comparison of POD Analyses Between Cases

The POD analysis applied to the 24° corner case that was presented in Fig. 11 is also applied to the 8° corner, 16° corner, 32° corner and boundary-layer cases and presented in figures 12, 13, 14 and 15, respectively.

Several characteristics of the POD analyses are common among each of the cases. For all cases, the POD modes only register interesting content within the boundary layer and shock layer. This is a sensible result as the freestream disturbances are small and

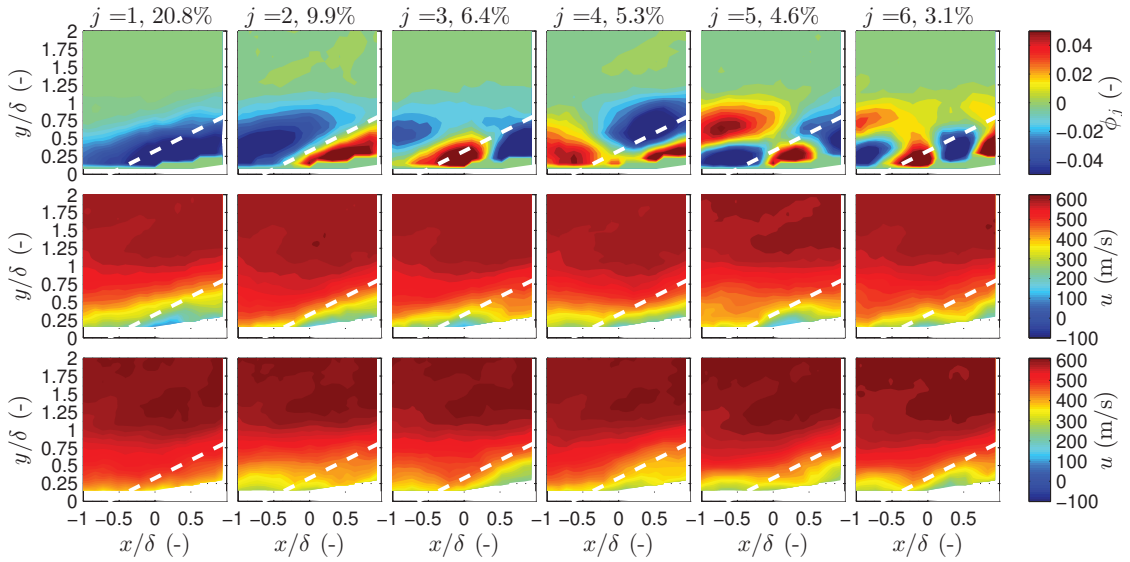

Fig. 12 Snapshot POD analysis for the 8° corner flow. Top row: POD modes are shown as contours of ϕ_j. Middle and bottom row: the mean streamwise velocity of snapshots that correspond to the largest positive and negative mode coefficients, respectively. A dashed white line denotes the mean shock location

incoherent relative to the disturbances within the shock and boundary layers. For mode number higher than approximately $j = 10$, the POD modes are difficult to distinguish from one case to another, besides the obvious change in boundary geometry. That is, the disturbances evident in the high order POD modes appear quite similar between cases in terms of distribution, amplitude, and length scale. To illustrate this point, the 30th POD mode (ϕ_{30}) is presented in Fig. 16 for each of the cases. The qualitative observation of commonality of the higher POD modes is also evident in the spectra of the eigenvalues presented in Fig. 9 (right). The initial thought was that the commonality of the higher order modes was due to noise in the measurement technique, which is also common among all cases. However, the signal-to-noise ratio appears sufficient at high mode number (Fig. 16).

Several characteristics of the POD analyses are dissimilar between the cases. In contrast to the 16°, 24° and 32° corner cases, the first POD of the 8° corner does not appear to indicate a relatively large separation bubble. Additionally, in the 24° and 32° cases, the shock wave appears to extend the upper boundary of where turbulent structures appear in the flow (Fig. 16, fourth and fifth panel from left). This is juxtaposed to the 8° and 16° cases where this is not readily observed (Fig. 16, second and third panel from left).

9 Conclusions

The shock-wave/boundary-layer interactions over four compression corners at $M_\infty = 2.8$ were investigated using one-dimensional KTV in the M3CT. The focus of this study was to use POD to characterize the effect of compression-corner angle on turbulent structure in Mach 2.8 flow. This canonical flow may be observed in practice as the deflection of a control surface on a vehicle in high-speed flight or in the flow path of a high-speed, air-breathing engine.

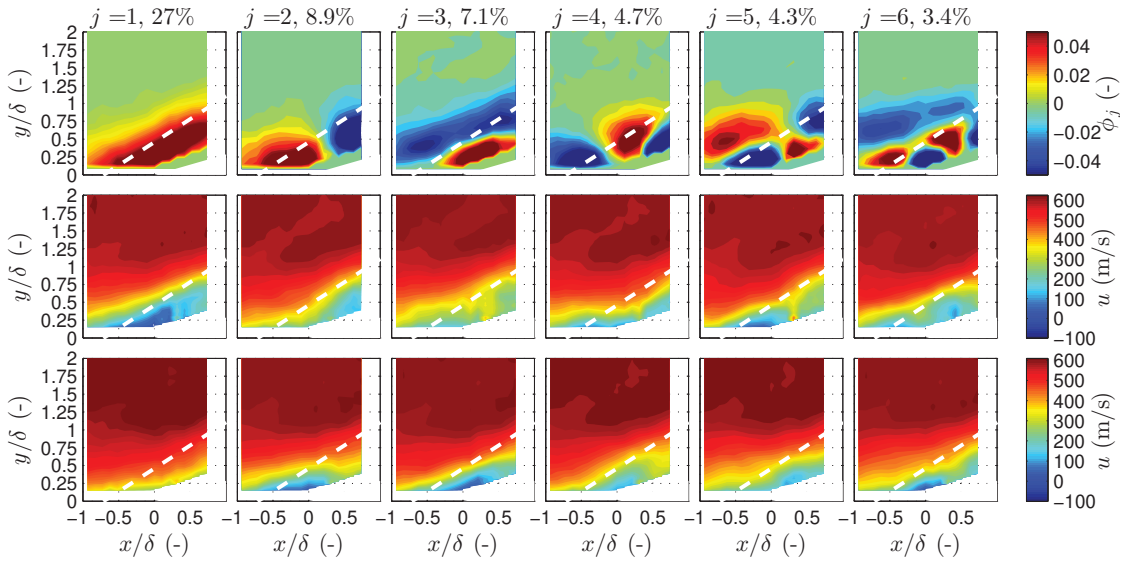

Fig. 13 Snapshot POD analysis for the 16° corner flow. Top row: POD modes are shown as contours of ϕ_j. Middle and bottom row: the mean streamwise velocity of snapshots that correspond to the largest positive and negative mode coefficients, respectively. A dashed white line denotes the mean shock location

Typical Z-type schlieren images were recorded for each compression-corner flow to address concerns about potential tunnel-starting issues in the M3CT. We found no such tunnel-starting issues and made fits to the mean initial shock-wave angle. These data agreed with data in the literature, which built confidence in studying these geometries in the M3CT.

For the shock-wave/turbulent boundary-layer interactions, data from ≈20 mean- and fluctuating-velocity profiles spanning ≈ 22 mm or $x/\delta \approx 2.1$ were recorded for compression-corner angles of 8°, 16°, 24°, and 32°. This was an effective demonstration of extending the application of tagging velocimetry into a complex flow field.

Proper orthogonal decomposition (POD) of the streamwise velocity data was used to examine the structures and spectra in the flow. Knight and Sirovich [83] and Moser [84] suggest that the POD eigenfunctions are a good set of basis functions with which to form an inertial-range spectrum for inhomogeneous, turbulent flows, and such a spectrum was identified in this work. That is, we found the POD eigenspectra to scale as $\lambda_j \propto j^{-11/9}$ which is analogous to the famous inertial-range scaling due to Kolmogorov [85] ($E \propto \epsilon^{2/3} k^{-5/3}$). At POD mode number greater than ≈ 10 there was an initially unanticipated similarity between the eigenspectra considering how dissimilar and inhomogeneous each case is (e.g., the boundary-layer flow vs. the 32° corner flow). However, upon close inspection, the first few POD modes do not clearly scale as $j^{-11/9}$, and these modes contain the structures (inhomogeneity and separation) which strongly modify the mean flow. Following the first ≈ 10 modes, the similarity of the inertial range is apparent between each case.

To identify the modification of the mean flow due to each POD mode, we presented the mean streamwise velocity of the samples which correspond to the POD mode coefficients falling above and below 1.5 standard deviations ($\pm 1.5\sigma$ of a_{ij}). We observed that the first several modes are somewhat similar between each compression corner case (with the

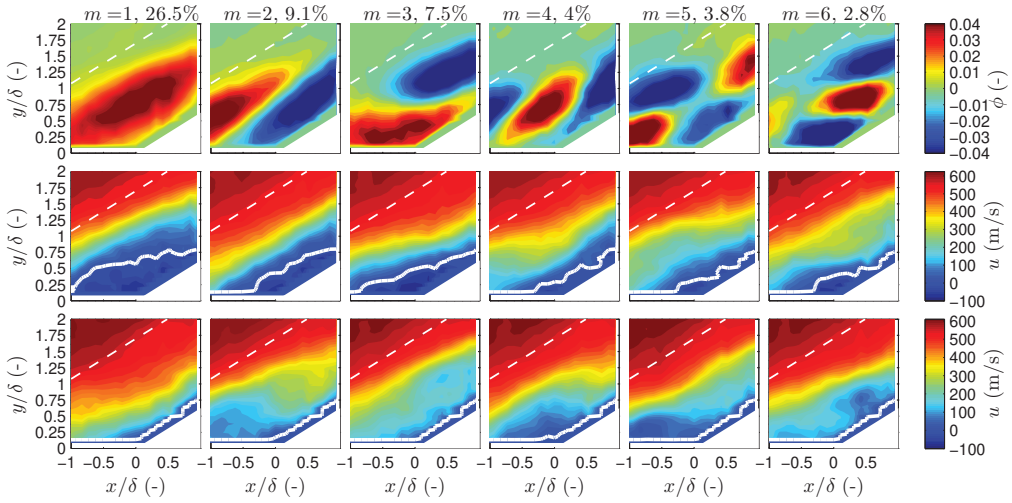

Fig. 14 Snapshot POD analysis for the 32° corner flow. Top row: POD modes are shown as contours of ϕ_j. Middle and bottom row: the mean streamwise velocity of snapshots that correspond to the largest positive and negative mode coefficients, respectively. A dashed white line denotes the mean shock location

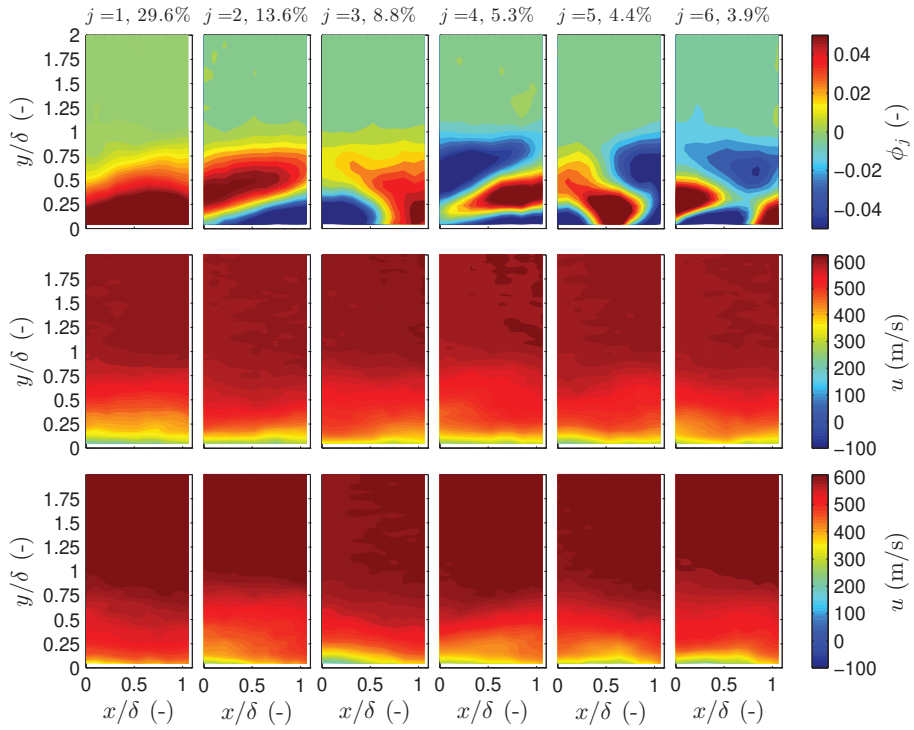

Fig. 15 Snapshot POD analysis for the boundary-layer flow. Each column corresponds to one of the first six POD modes marked by the mode number j and the fraction of energy associated with each mode in %. Top row: POD modes are shown as contours of ϕ_j. Middle and bottom row: the mean streamwise velocity of snapshots that correspond to the largest positive and negative mode coefficients, respectively

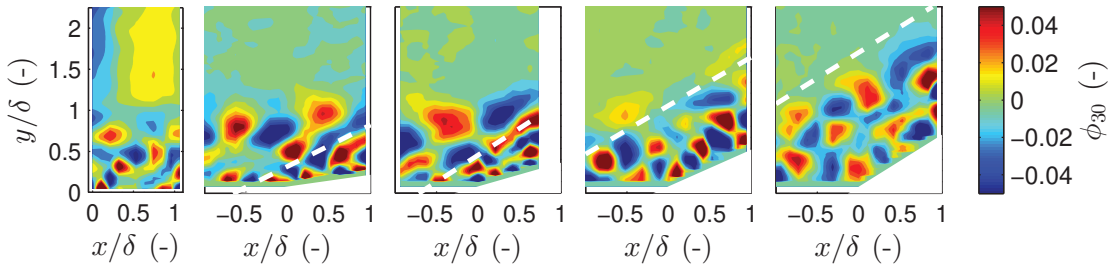

Fig. 16 Comparison of the 30th POD mode (ϕ_{30}) among the boundary-layer and 8°, 16°, 24°, and 32° corner flows, from left to right, respectively. A dashed white line denotes the mean shock location

exception of the 8° corner where the flow was mostly attached). These first POD modes contain most of the kinetic energy and are those that modify the mean flow, giving rise to features such as separation bubble filling/collapse and oscillation.

Acknowledgments

The M3CT facilities were supplied by the Arnold Engineering Development Complex (AEDC). The Air Force Summer Faculty Fellowship Program (SFFP) supported Mustafa and Parziale with a stipend for this work. Mustafa and Parziale were supported by AFOSR Young Investigator Program Grant FA9550-16-1-0262 and equipment for this work was supported by AFOSR DURIP Grant FA9550-15-1-0325; Ivett Leyva of AFOSR is the Program Manager for both grants. We acknowledge the machine work done by Milan Simonovic and Marshall Reid of Stevens Institute of Technology. We also would like to thank Jonathan Brooks of University of Maryland for assistance with operating the wind tunnel and the Pitot measurements. We would like to acknowledge the encouragement of John Laffery and Dan Marren of AEDC White Oak.

References

[1] D. S. Dolling, "Fifty Years of Shock-Wave/Boundary-Layer Interaction Research: What next?" *AIAA Journal*, vol. 39, no. 8, pp. 1517–1531, 2001.

[2] B. Wang, N. D. Sandham, Z. Hu, and W. Liu, "Numerical study of oblique shock-wave/boundary-layer interaction considering sidewall effects," *Journal of Fluid Mechanics*, vol. 767, pp. 526–561, 2015.

[3] B. John, V. N. Kulkarni, and G. Natarajan, "Shock wave boundary layer interactions in hypersonic flows," *International Journal of Heat and Mass Transfer*, vol. 70, pp. 81–90, 2014.

[4] N. A. Adams, "Direct simulation of the turbulent boundary layer along a compression ramp at $m = 3$ and $\mathrm{re}_\Theta = 1685$," *Journal of Fluid Mechanics*, vol. 420, pp. 47–83, 2000.

[5] M. Wu and M. P. Martin, "Direct Numerical Simulation of Supersonic Turbulent Boundary Layer Over a Compression Ramp," *AIAA Journal*, vol. 45, no. 4, pp. 879–889, 2007.

[6] Wu, M. and Martin, M. P., "Analysis of shock motion in shockwave and turbulent boundary layer interaction using direct numerical simulation data," *Journal of Fluid Mechanics*, vol. 594, pp. 71–83, 2008.

[7] R. H. M. Giepman, F. F. J. Schrijer, and B. W. van Oudheusden, "High-resolution PIV measurements of a transitional shock wave-boundary layer interaction," *Experiments in Fluids*, vol. 56, no. 6, p. 113, 2015.

[8] G. S. Settles, I. E. Vas, and S. M. Bogdonoff, "Details of a Shock-Separated Turbulent Boundary Layer at a Compression Corner," *AIAA Journal*, vol. 14, no. 12, pp. 1709–1715, 1976.

[9] G. S. Settles, T. J. Fitzpatrick, and S. M. Bogdonoff, "Detailed Study of Attached and Separated Compression Corner Flowfields in High Reynolds Number Supersonic Flow," *AIAA Journal*, vol. 17, no. 6, pp. 579–585, 1979.

[10] A. J. Smits and K.-C. Muck, "Experimental study of three shock wave/turbulent boundary layer interactions," *Journal of Fluid Mechanics*, vol. 182, pp. 291–314, 1987.

[11] R. A. Humble, F. Scarano, and B. W. van Oudheusden, "Particle image velocimetry measurements of a shock wave/turbulent boundary layer interaction," *Experiments in Fluids*, vol. 43, no. 2-3, pp. 173–183, 2007.

[12] R. A. Humble, G. E. Elsinga, F. Scarano, and B. W. van Oudheusden, "Three-dimensional instantaneous structure of a shock wave/turbulent boundary layer interaction," *Journal of Fluid Mechanics*, vol. 622, pp. 33–62, 2009.

[13] D. V. Gaitonde, "Progress in shock wave/boundary layer interactions," *Progress in Aerospace Sciences*, vol. 72, pp. 80–99, 2015.

[14] G. S. Settles and L. J. Dodson, "Hypersonic Shock/Boundary-Layer Interaction Database: New and Corrected Data," NASA CR 177638, 1994.

[15] D. Knight, H. Yan, A. G. Panaras, and A. Zheltovodov, "Advances in CFD prediction of shock wave turbulent boundary layer interactions," *Progress in Aerospace Sciences*, vol. 39, no. 2, pp. 121–184, 2003.

[16] H. Babinsky and J. K. Harvey, Eds., *Shock Wave-Boundary-Layer Interactions*, 1st ed. Cambridge University Press, 2011.

[17] H. Tennekes and J. L. Lumley, *A First Course in Turbulence*. MIT press, 1972.

[18] J. L. Lumley, "The structure of inhomogeneous turbulent flows," in *Atmospheric Turbulence and Radio Wave Propagation*, A. M. Yaglom and V. I. Tatarsky, Eds., 1967, pp. 166–176.

[19] G. Berkooz, P. Holmes, and J. L. Lumley, "The Proper Orthogonal Decomposition in the Analysis of Turbulent Flows," *Annual Review of Fluid Mechanics*, vol. 25, no. 1, pp. 539–575, 1993.

[20] K. Taira, S. L. Brunton, S. T. . M. Dawson, C. W. Rowley, T. Colonius, B. J. McKeon, O. T. Schmidt, S. Gordeyev, V. Theofilis, and L. S. Ukeiley, "Modal Analysis of Fluid Flows: An Overview," *AIAA Journal*, pp. 1–29, 2017.

[21] H. Chen, D. L. Reuss, and V. Sick, "On the use and interpretation of proper orthogonal decomposition of in-cylinder engine flows," *Measurement Science and Technology*, vol. 23, no. 8, p. 085302, 2012. [Online]. Available: http://stacks.iop.org/0957-0233/23/i=8/a=085302

[22] H. Chen, D. L. Reuss, D. L. Hung, and V. Sick, "A practical guide for using proper orthogonal decomposition in engine research," *International Journal of Engine Research*, vol. 14, no. 4, pp. 307–319, 2013.

[23] P. Druault, P. Guibert, and F. Alizon, "Use of proper orthogonal decomposition for time interpolation from PIV data," *Experiments in Fluids*, vol. 39, no. 6, pp. 1009–1023, Dec 2005.

[24] A. Orellano and H. Wengle, "Pod analysis of coherent structures in forced turbulent flow over a fence," *Journal of Turbulence*, vol. 2, p. N8, 2001.

[25] N. Murray, E. Sällström, and L. Ukeiley, "Properties of subsonic open cavity flow fields," *Physics of Fluids*, vol. 21, no. 9, p. 095103, 2009.

[26] J. P. Bonnet, D. R. Cole, J. Delville, M. N. Glauser, and L. S. Ukeiley, "Stochastic estimation and proper orthogonal decomposition: Complementary techniques for identifying structure," *Experiments in Fluids*, vol. 17, no. 5, pp. 307–314, Sep 1994.

[27] J. H. Tu, C. W. Rowley, J. N. Kutz, and J. K. Shang, "Spectral analysis of fluid flows using sub-nyquist-rate piv data," *Experiments in Fluids*, vol. 55, no. 9, Sep 2014. [Online]. Available: https://doi.org/10.1007/s00348-014-1805-6

[28] S. Piponniau, E. Collin, P. Dupont, and J. Debiève, "Reconstruction of velocity fields from wall pressure measurements in a shock wave/turbulent boundary layer interaction," *International Journal of Heat and Fluid Flow*, vol. 35, pp. 176–186, 2012.

[29] D. Zahradka, N. J. Parziale, M. S. Smith, and E. C. Marineau, "Krypton tagging velocimetry in a turbulent mach 2.7 boundary layer," *Experiments in Fluids*, vol. 57, p. 62, 2016.

[30] M. A. Mustafa, M. B. Hunt, N. J. Parziale, M. S. Smith, and E. C. Marineau, "Krypton Tagging Velocimetry (KTV) Investigation of Shock-Wave/Turbulent Boundary-Layer Interaction," in *Proceedings of AIAA SciTech 2017*. Grapevine, Texas: AIAA-2017-0025, 9-13 January 2017.

[31] G. S. Settles, *Schlieren and Shadowgraph Techniques*, First ed. Springer-Verlag Berlin Heidelberg, 2001.

[32] F. W. Spaid and J. C. Frishett, "Incipient Separation of a Supersonic, Turbulent Boundary Layer, Including Effects of Heat Transfer," *AIAA*, vol. 10, no. 7, pp. 915–922, 1972.

[33] J. Haertig, M. Havermann, C. Rey, and A. George, "Particle Image Velocimetry in Mach 3.5 and 4.5 Shock-Tunnel Flows," *AIAA Journal*, vol. 40, no. 6, pp. 1056–1060, 2002.

[34] E. Loth, "Compressibility and Rarefaction Effects on Drag of a Spherical Particle," *AIAA Journal*, vol. 46, no. 9, pp. 2219–2228, 2008.

[35] A. G. Hsu, R. Srinivasan, R. D. W. Bowersox, and S. W. North, "Molecular Tagging Using Vibrationally Excited Nitric Oxide in an Underexpanded Jet Flowfield," *AIAA Journal*, vol. 47, no. 11, pp. 2597–2604, 2009.

[36] Hsu, A. G. and Srinivasan, R. and Bowersox, R. D. W. and North, S. W., "Two-component molecular tagging velocimetry utilizing NO fluorescence lifetime and NO_2 photodissociation techniques in an underexpanded jet flowfield," *Applied Optics*, vol. 48, no. 22, pp. 4414–4423, 2009.

[37] R. Sánchez-González, R. Srinivasan, R. D. W. Bowersox, and S. W. North, "Simultaneous velocity and temperature measurements in gaseous flow fields using the venom technique," *Optics Letters*, vol. 36, no. 2, pp. 196–198, 2011.

[38] R. Sánchez-González, R. D. W. Bowersox, and S. W. North, "Simultaneous velocity and temperature measurements in gaseous flowfields using the vibrationally excited nitric oxide monitoring technique: a comprehensive study," *Applied Optics*, vol. 51, no. 9, pp. 1216–1228, 2012.

[39] Sánchez-González, R. and Bowersox, R. D. W. and North, S. W., "Vibrationally excited NO tagging by $NO(A^2\Sigma^+)$ fluorescence and quenching for simultaneous velocimetry and thermometry in gaseous flows," *Optics Letters*, vol. 39, no. 9, pp. 2771–2774, 2014.

[40] N. Dam, R. J. H. Klein-Douwel, N. M. Sijtsema, and J. J. ter Meulen, "Nitric oxide flow tagging in unseeded air," *Optics Letters*, vol. 26, no. 1, pp. 36–38, 2001.

[41] N. M. Sijtsema, N. J. Dam, R. J. H. Klein-Douwel, and J. J. ter Meulen, "Air Photolysis and Recombination Tracking: A New Molecular Tagging Velocimetry Scheme," *AIAA Journal*, vol. 40, no. 6, pp. 1061–1064, 2002.

[42] W. P. N. Van der Laan, R. A. L. Tolboom, N. J. Dam, and J. J. ter Meulen, "Molecular tagging velocimetry in the wake of an object in supersonic flow," *Experiments in Fluids*, vol. 34, no. 4, pp. 531–534, 2003.

[43] R. Miles, C. Cohen, J. Connors, P. Howard, S. Huang, E. Markovitz, and G. Russell, "Velocity measurements by vibrational tagging and fluorescent probing of oxygen," *Optics Letters*, vol. 12, no. 11, pp. 861–863, 1987.

[44] R. Miles, J. Connors, E. Markovitz, P. Howard, and G. Roth, "Instantaneous profiles and turbulence statistics of supersonic free shear layers by Raman excitation plus laser-induced electronic fluorescence (RELIEF) velocity tagging of oxygen," *Experiments in Fluids*, vol. 8, no. 1-2, pp. 17–24, 1989.

[45] R. B. Miles, D. Zhou, B. Zhang, and W. R. Lempert, "Fundamental Turbulence Measurements by RELIEF Flow Tagging," *AIAA Journal*, vol. 31, no. 3, pp. 447–452, 1993.

[46] R. B. Miles and W. R. Lempert, "Quantitative Flow Visualization in Unseeded Flows," *Annual Review of Fluid Mechanics*, vol. 29, no. 1, pp. 285–326, 1997.

[47] R. B. Miles, J. Grinstead, R. H. Kohl, and G. Diskin, "The RELIEF flow tagging technique and its application in engine testing facilities and for helium-air mixing studies," *Measurement Science and Technology*, vol. 11, no. 9, pp. 1272–1281, 2000.

[48] J. B. Michael, M. R. Edwards, A. Dogariu, and R. B. Miles, "Femtosecond laser electronic excitation tagging for quantitative velocity imaging in air," *Applied Optics*, vol. 50, no. 26, pp. 5158–5162, 2011.

[49] M. R. Edwards, A. Dogariu, and R. B. Miles, "Simultaneous Temperature and Velocity Measurements in Air with Femtosecond Laser Tagging," *AIAA Journal*, vol. 53, no. 8, pp. 2280–2288, 2015.

[50] N. Jiang, B. R. Halls, H. U. Stauffer, P. M. Danehy, J. R. Gord, and S. Roy, "Selective two-photon absorptive resonance femtosecond-laser electronic-excitation tagging velocimetry," *Optics Letters*, vol. 41, no. 10, pp. 2225–2228, 2016.

[51] N. Jiang, J. G. Mance, M. N. Slipchenko, J. J. Felver, H. U. Stauffer, T. Yi, P. M. Danehy, and S. Roy, "Seedless velocimetry at 100 khz with picosecond-laser electronic-excitation tagging," *Optics Letters*, vol. 42, no. 2, pp. 239–242, 2017.

[52] J. L. Mills, "Investigation of Multi-Photon Excitation in Argon with Applications in Hypersonic Flow Diagnostics," Ph.D. dissertation, Old Dominion University, 2016.

[53] J. C. McDaniel, B. Hiller, and R. K. Hanson, "Simultaneous multiple-point velocity measurements using laser-induced iodine fluorescence," *Optics Letters*, vol. 8, no. 1, pp. 51–53, 1983.

[54] R. J. Balla, "Iodine Tagging Velocimetry in a Mach 10 Wake," *AIAA Journal*, vol. 51, no. 7, pp. 1–3, 2013.

[55] P. Barker, A. Bishop, and H. Rubinsztein-Dunlop, "Supersonic velocimetry in a shock tube using laser enhanced ionisation and planar laser induced fluorescence," *Applied Physics B*, vol. 64, no. 3, pp. 369–376, 1997.

[56] W. R. Lempert, N. Jiang, S. Sethuram, and M. Samimy, "Molecular Tagging Velocimetry Measurements in Supersonic Microjets," *AIAA Journal*, vol. 40, no. 6, pp. 1065–1070, 2002.

[57] W. R. Lempert, M. Boehm, N. Jiang, S. Gimelshein, and D. Levin, "Comparison of molecular tagging velocimetry data and direct simulation monte carlo simulations in supersonic micro jet flows," *Experiments in Fluids*, vol. 34, no. 3, pp. 403–411, 2003.

[58] T. Handa, K. Mii, T. Sakurai, K. Imamura, S. Mizuta, and Y. Ando, "Study on supersonic rectangular microjets using molecular tagging velocimetry," *Experiments in Fluids*, vol. 55, no. 5, pp. 1–9, 2014.

[59] S. Zhang, X. Yu, H. Yan, H. Huang, and H. Liu, "Molecular tagging velocimetry of NH fluorescence in a high-enthalpy rarefied gas flow," *Applied Physics B*, vol. 123, no. 4, p. 122, 2017.

[60] L. R. Boedeker, "Velocity measurement by H_2O photolysis and laser-induced fluorescence of OH," *Optics Letters*, vol. 14, no. 10, pp. 473–475, 1989.

[61] J. A. Wehrmeyer, L. A. Ribarov, D. A. Oguss, and R. W. Pitz, "Flame Flow Tagging Velocimetry with 193-nm H_2O Photodissociation," *Applied Optics*, vol. 38, no. 33, pp. 6912–6917, 1999.

[62] R. W. Pitz, M. D. Lahr, Z. W. Douglas, J. A. Wehrmeyer, S. Hu, C. D. Carter, K.-Y. Hsu, C. Lum, and M. M. Koochesfahani, "Hydroxyl tagging velocimetry in a supersonic flow over a cavity," *Applied Optics*, vol. 44, no. 31, pp. 6692–6700, 2005.

[63] M. A. André, P. M. Bardet, R. A. Burns, and P. M. Danehy, "Characterization of hydroxyl tagging velocimetry for low-speed flows," *Measurement Science and Technology*, vol. 28, no. 8, p. 085202, 2017.

[64] B. Hiller, R. A. Booman, C. Hassa, and R. K. Hanson, "Velocity visualization in gas flows using laser-induced phosphorescence of biacetyl," *Review of Scientific Instruments*, vol. 55, no. 12, pp. 1964–1967, 1984.

[65] C. P. Gendrich and M. M. Koochesfahani, "A spatial correlation technique for estimating velocity fields using molecular tagging velocimetry (MTV)," *Experiments in Fluids*, vol. 22, no. 1, pp. 67–77, 1996.

[66] C. P. Gendrich, M. M. Koochesfahani, and D. G. Nocera, "Molecular tagging velocimetry and other novel applications of a new phosphorescent supramolecule," *Experiments in Fluids*, vol. 23, no. 5, pp. 361–372, 1997.

[67] B. Stier and M. M. Koochesfahani, "Molecular tagging velocimetry (MTV) measurements in gas phase flows," *Experiments in Fluids*, vol. 26, no. 4, pp. 297–304, 1999.

[68] L. A. Ribarov, J. A. Wehrmeyer, F. Batliwala, R. W. Pitz, and P. A. DeBarber, "Ozone Tagging Velocimetry Using Narrowband Excimer Lasers," *AIAA Journal*, vol. 37, no. 6, pp. 708–714, 1999.

[69] M. A. André, R. A. Burns, P. M. Danehy, S. R. Cadell, B. G. Woods, and P. M. Bardet, "Development of N_2O-MTV for low-speed flow and in-situ deployment to an integral effect test facility," *Experiments in Fluids*, vol. 59, no. 1, p. 14, 2018.

[70] J. L. Mills, C. I. Sukenik, and R. J. Balla, "Hypersonic Wake Diagnostics Using Laser Induced Fluorescence Techniques," in *Proceedings of 42nd AIAA Plasmadynamics and Lasers Conference*. Honolulu, Hawaii: AIAA 2011-3459, 2011.

[71] R. J. Balla and J. L. Everhart, "Rayleigh Scattering Density Measurements, Cluster Theory, and Nucleation Calculations at Mach 10," *AIAA Journal*, vol. 50, no. 3, pp. 698–707, 2012.

[72] N. J. Parziale, M. S. Smith, and E. C. Marineau, "Krypton Tagging Velocimetry for Use in High-Speed Ground-Test Facilities," in *Proceedings of AIAA SciTech 2015*. Kissimmee, Florida: AIAA-2015-1484, 5-9 January 2015.

[73] ——, "Krypton tagging velocimetry of an underexpanded jet," *Applied Optics*, vol. 54, no. 16, pp. 5094–5101, 2015.

[74] D. Zahradka, N. J. Parziale, M. S. Smith, and E. C. Marineau, "Krypton Tagging Velocimetry (KTV) in Supersonic Turbulent Boundary Layers," in *Proceedings of AIAA SciTech 2016*. San Diego, California: AIAA-2016-1587, 7-11 January 2016.

[75] M. A. Mustafa, N. J. Parziale, M. S. Smith, and E. C. Marineau, "Amplification and structure of streamwise-velocity fluctuations in compression-corner shock-wave/turbulent boundary-layer interactions," *Journal of Fluid Mechanics*, vol. 863, pp. 1091–1122, 2019.

[76] M. A. Mustafa, D. Shektman, and N. J. Parziale, "Single-Laser Krypton Tagging Velocimetry (KTV) Investigation of Air and N2 Boundary-Layer Flows Over a Hollow Cylinder in the Stevens Shock Tube," in *Proceedings of AIAA Scitech 2019*. San Diego, California: AIAA-2019-1820, 7-11 January 2019.

[77] Mustafa, M. A. and Parziale, N. J. and Smith, M. S. and Marineau, E. C., "Nonintrusive Freestream Velocity Measurement in a Large-Scale Hypersonic Wind Tunnel," *AIAA Journal*, vol. 55, no. 10, pp. 3611–3616, 2017.

[78] R. S. F. Chang, H. Horiguchi, and D. W. Setser, "Radiative lifetimes and two-body collisional deactivation rate constants in argon for Kr($4p^5 5p$) and Kr($4p^5 5p'$) states," *The Journal of Chemical Physics*, vol. 73, no. 2, pp. 778–790, 1980.

[79] T. O'Haver, *A Pragmatic Introduction to Signal Processing*. University of Maryland at College Park, 1997.

[80] L. Sirovich, "Turbulence and the Dynamics of Coherent Structures, Part I: Coherent Structures," *Quarterly of Applied Mathematics*, vol. 45, no. 3, pp. 561–571, 1987.

[81] M. Stöhr, R. Sadanandan, and W. Meier, "Phase-resolved characterization of vortex–flame interaction in a turbulent swirl flame," *Experiments in Fluids*, vol. 51, no. 4, pp. 1153–1167, 2011.

[82] C. W. Rowley, T. Colonius, and R. M. Murray, "Model reduction for compressible flows using pod and galerkin projection," *Physica D: Nonlinear Phenomena*, vol. 189, no. 1-2, pp. 115–129, 2004.

[83] B. Knight and L. Sirovich, "Kolmogorov Inertial Range for Inhomogeneous Turbulent Flows," *Physical Review Letters*, vol. 65, no. 11, pp. 1356–1359, 1990.

[84] R. D. Moser, "Kolmogorov inertial range spectra for inhomogeneous turbulence," *Physics of Fluids*, vol. 6, no. 2, pp. 794–801, 1994.

[85] A. N. Kolmogorov, "The local structure of turbulence in incompressible viscous fluid for very large Reynolds numbers," vol. 30, no. 4, pp. 299–303, 1941.

[86] J. M. Brooks, A. K. Gupta, M. S. Smith, and E. C. Marineau, "PIV Measurements of Mach 2.7 Turbulent Boundary Layer with varying Reynolds Numbers," in *Proceedings of 54th Aerospace Sciences Meeting, SciTech*. San Diego, California: AIAA-2016-1147, 2016.

[87] N. T. Clemens and V. Narayanaswamy, "Low-frequency unsteadiness of shock wave/turbulent boundary layer interactions," *Annual Review of Fluid Mechanics*, vol. 46, pp. 469–492, 2014.